Surfaces and Interfaces 96 (2026) 109929

Contents lists available at ScienceDirect

Surfaces and Interfaces

journal homepage: www.sciencedirect.com/journal/surfaces-and-interfaces

Scalable slot-die coating of dipole-engineered self-assembled monolayers for efficient large-area perovskite photovoltaics

Chia-Feng Li [a,b], Shih-Han Huang [c], Sheng-Wen Huang [d], You-Ren Chen [b], Hou-Chin Cha [c,e], Pin-Hao Chao [b], Feng-Yu Tsai [a,*], Yu-Ching Huang [b,c,f,g,*]

[a] Department of Materials Science and Engineering, National Taiwan University, Taipei 10617, Taiwan
[b] Department of Materials Engineering, Ming Chi University of Technology, New Taipei City, 24301, Taiwan
[c] Organic Electronics Research Center, Ming Chi University of Technology, New Taipei City 24301, Taiwan
[d] Green Energy & Environment Research Laboratories, Industrial Technology Research Institute (ITRI), Tainan, 71150, Taiwan
[e] College of Engineering, Ming Chi University of Technology, New Taipei City 24301, Taiwan
[f] Research Center for Critical Issues, Academia Sinica, Taipei, 115201, Taiwan
[g] Center for Sustainability and Energy Technologies, Chang Gung University, Taoyuan City, 33302, Taiwan

ARTICLE INFO

Keywords:
Self-assembled monolayers
Interface
Slot-die
Ambient
Module

ABSTRACT

Self-assembled monolayers (SAMs) are increasingly employed as ultrathin functional coatings for regulating surface energetics in advanced thin-film technologies. However, achieving simultaneous control over molecular ordering, interfacial robustness, and film uniformity remains a critical challenge, particularly when transitioning from lab-scale processes to scalable slot-die coating. In this work, we systematically investigate the role of small carboxylic acid additives in regulating the coating quality and electronic structure of MeO-2PACz monolayers. By introducing acetic acid (AcOH) and trifluoroacetic acid (TFA) as surface modulators, we elucidate how subtle chemical variations govern nanoscale packing behavior and work-function tuning. The TFA-modified coating exhibits a significantly more ordered molecular arrangement and enhanced surface hydrophobicity (contact angle ~67.4°), indicating superior film homogeneity. To validate the scalability and coating uniformity, the optimized SAMs were integrated into large-area (5 × 5 cm^2) multilayer thin-film modules using a slot-die coating process. Under accelerated thermal–humidity aging conditions, the additive-engineered interfaces demonstrated superior robustness, retaining 65% of their initial function. Furthermore, the optimized slot-die coated modules achieved a power conversion efficiency of 14.72%, confirming that the proposed dipole-engineering strategy effectively translates high coating quality into macroscopic device performance. Overall, this study provides a process-compatible guideline for designing robust, large-area interfacial coatings suitable for scalable manufacturing in advanced thin-film systems.

1. Introduction

Perovskite solar cells (PSCs) have garnered significant attention over the past decade as one of the most promising next-generation photovoltaic technologies. Owing to their exceptional optoelectronic properties, low fabrication cost, and compatibility with flexible and lightweight substrates, PSCs have emerged as leading contenders in solar energy research [1,2]. Through continuous advances in material design and interface engineering, the power conversion efficiency (PCE) of single-junction PSCs has reached 27.0% [3]. Recently, self-assembled monolayers (SAMs) have gained prominence as effective hole-selective materials for inverted PSC architectures [4–6]. With their precisely engineered molecular architectures and tunable interfacial dipoles, SAMs enable highly efficient hole extraction when integrated as interfacial modifiers or hole-selective layers [7,8]. This molecular-level control over interfacial energetics promotes favorable band alignment and reduces nonradiative recombination losses, thereby contributing to improved photovoltaic performance. Consequently, SAM-based interface engineering has become a pivotal strategy for boosting the efficiency, stability, and scalability of perovskite photovoltaics. While phosphonic acid-based SAMs have significantly advanced hole transport layer engineering in perovskite photovoltaics, critical fundamental uncertainties remain that impede their transition from laboratory research to industrial scale-up [9]. To address these scalable processing

* Corresponding authors at: Department of Materials Engineering, Ming Chi University of Technology, New Taipei City, 24301, Taiwan.
E-mail addresses: ftsai@ntu.edu.tw (F.-Y. Tsai), huangyc@mail.mcut.edu.tw (Y.-C. Huang).

https://doi.org/10.1016/j.surfin.2026.109929
Received 15 January 2026; Received in revised form 18 June 2026; Accepted 22 June 2026
Available online 23 June 2026

challenges, a recent study has demonstrated that a NiO_X/mesoporous Al_2O_3 scaffold enables large-area SAM deposition via dip coating, effectively eliminating interfacial voids and passivating buried defects. This approach achieves a champion mini-module efficiency of 22.66% under ambient conditions, providing a robust route toward scalable and stable PSCs [10].

Despite these advantages, the practical deposition of high-quality SAMs remains a critical challenge, as conventional molecules often fail to assemble into dense and uniform monolayers. Their structurally simplistic frameworks, single anchoring functionalities, and weak intermolecular interactions can lead to molecular aggregation rather than ordered packing. This results in incomplete surface coverage, inefficient hole extraction, and detrimental non-radiative recombination at the perovskite/HTL interface [11–13]. To mitigate these assembly limitations, various strategies focusing on molecular design and surface activation have been proposed. For instance, Zeng et al. reported a SAM molecule integrating a donor–acceptor unit with a phosphonic acid anchoring group. This molecule forms a face-on π-stacked configuration on transparent conductive substrates, exhibiting strong affinity toward multicrystalline perovskite surfaces. Such molecular architecture not only enhances interfacial contact but also effectively passivates the buried interface, leading to substantial improvements in both PCE and stability [14]. Similarly, Li et al. designed a multifunctional π-conjugated molecule with a spirofluorene-bridged backbone, which enables strong π–π stacking with carbazole-based SAMs, resulting in a more compact and well-covered interfacial layer. The incorporated methoxy groups can coordinate with undercoordinated Pb^{2+}, effectively passivating interfacial defects, while the triphenylamine units facilitate more efficient hole transport [15]. Beyond molecular design, Luo et al. developed a rapid 15 s hydroxylation strategy for indium tin oxide (ITO) that enhances SAM anchoring and eliminates conventional pretreatment. This process simultaneously forms nanoscale antireflective structures, enabling PSCs with PCE of 26.6% and excellent thermal stability [16].

On the other hand, an effective approach to address these assembly challenges is the construction of co-assembled SAMs (Co-SAMs) [17]. For instance, Ding et al. reported a molecular doping strategy that integrates methyl 3-chlorosulfonyl-2-thiophenecarboxylate (MCC) into Me-4PACz SAMs. The multifunctional MCC molecule enhances SAM packing, surface uniformity, and interfacial passivation through synergistic dipole regulation, Pb^{2+} coordination, and improved surface wettability, thereby promoting high-quality perovskite crystallization [18]. Song et al. introduced a sequentially deposited Co-SAM layer with precise controlled nanostructures, resulting in optimized energy-level alignment [19]. He et al. demonstrated that incorporating benzylphosphonic acid (BPPA) into Me-4PACz aligns the energy levels at the HTL/perovskite interface, thereby minimizing charge accumulation [20]. Similarly, Cheng et al. proposed a co-adsorption strategy utilizing 2-chloro-5-(trifluoromethyl)isonicotinic acid (PyCA-3F) at the 2PACz interface, which improves perovskite crystallinity and reduces trap density, enabling a PCE exceeding 25% [21]. In addition, Yan et al. further demonstrated that co-assembling Me-4PACz with phosphorylcholine chloride significantly improves monolayer coverage and passivates defects via dual-functional groups, which accelerates charge transport [22]. Collectively, these studies demonstrate that Co-SAM strategies can significantly enhance interfacial contact, defect passivation, and charge extraction in inverted PSCs. However, although significant progress has been made in developing SAMs for perovskite solar cells, most reported studies still rely on lab-scale spin-coating processes. Systematic investigations into scalable fabrication techniques, such as slot-die coating, remain limited [23,24]. Since large-area coating kinetics differ fundamentally from spin-coating, addressing this limitation is essential for translating SAM-based technologies toward industrially relevant applications.

In this study, we systematically evaluate the effects of incorporating different small molecules into MeO-2PACz solutions to optimize the coating quality and electronic homogeneity. Among the investigated additives, trifluoroacetic acid (TFA) is identified as an effective surface modulator for improving the phase uniformity of MeO-2PACz films. Owing to its intrinsic dipole orientation, TFA interacts with MeO-2PACz molecules to downshift the highest occupied molecular orbital (HOMO) level, while simultaneously suppressing excessive molecular aggregation. This synergistic effect promotes the formation of a homogeneous, defect-free, and energetically well-aligned hole-transporting layer (HTL). In addition, the incorporation of TFA significantly enhances charge transport and effectively suppresses non-radiative recombination in the resulting films. To demonstrate the industrial relevance of this coating strategy, we validate its performance in scalable slot-die coating processes. The optimized coating enables the fabrication of devices with excellent operational stability (maintaining 65% of initial performance for over 120 h). Furthermore, the integrated large-area perovskite solar modules (PSMs) achieve a high functional efficiency of 14.72%, confirming the potential of this strategy for mass-production coating applications.

2. Experimentals

2.1. Materials

[2-(3,6-Dimethoxy-9H-carbazol-9-yl)ethyl]phosphonic Acid (MeO-2PACz, >98.0%), trifluoroacetic acid (TFA, >99.0%), lead iodide (PbI_2, 99.99%), bathocuproine (BCP, >99%), and propylamine hydrochloride (PACl, >98.0%) were purchased from TCI. methylammonium chloride (MACl, 99.99%), Formamidinium Iodide (FAI, 99.99%) were obtained from Greatcell solar materials. Rubidium iodide (RbI, 99.9%), cesium iodide (CsI, 99.99%), dimethyl sulfoxide (DMSO, 99.9%), dimethylformamide (DMF, ≥99.9%), chlorobenzene (CB, 99.9%), ethyl alcohol (EtOH, 99.0%), and isopropanol (IPA, 99.5%) were obtained from Sigma-Aldrich. 2-thiopheneethylamine, hydrochloride (TEACl) solution was purchased from FMPV. All reagents and solvents were used in their purchased form without further treatment.

2.2. Fabrication procedure

FTO-coated glass substrates were cleaned ultrasonically by sequential washing with acetone, methanol, and isopropanol for 20 min each, followed by drying with nitrogen gas. The MeO-2PACz HTL solution (1 mM in EtOH) was spin-coated onto the cleaned FTO glass at 3000 rpm for 30 s, followed by thermal treatment at 100 °C for 5 min. For the modified HTLs, different concentrations of TFA were incorporated into the MeO-2PACz solution prior to deposition. The perovskite precursor solution was prepared according to a previously published procedure [25]. 70 μL of the precursor solution was deposited onto the HTL film and spin-coated at 5000 rpm for 30 s inside a nitrogen-filled glove box. After spinning for 18 s, 500 μL of ethyl acetate was dripped onto the rotating sample to induce rapid crystallization and form a transparent intermediate phase. The films were then annealed on a hot plate at 150 °C for 10 min to obtain dark-brown perovskite films. The passivation layer was prepared by dissolving TEACl (4 mM) in IPA. 70 μL of the passivation solution was spin-coated onto the perovskite layer at 3000 rpm for 30 s. The electron transport layer (ETL) was prepared by dissolving $PC_{61}BM$ (20 mg) in 1 mL of CB, and 70 μL of the ETL solution was spin-coated onto the passivation layer at 1000 rpm for 30 s. A thin BCP interlayer was then introduced by spin-coating 70 μL of a 0.5 mg/mL IPA solution at 3000 rpm for 30 s. Device fabrication was completed by thermally evaporating a 100 nm silver electrode under high-vacuum conditions ($< 5 \times 10^{-6}$ Pa).

For the scalable fabrication process, the HTL was deposited via slot-die coating under optimized conditions to ensure defect-free film formation over large areas. The coating gap was precisely controlled at 200–250 μm, while the substrate temperature was maintained at 65 °C. The coating speed and solution feeding rate were synchronized at 1.5 m

min^{-1} and 1.5 mL min^{-1}, respectively. These parameters were critical to maintain meniscus stability and ensure uniform wet-film formation across the large-area substrate. Notably, the heated substrate (65 °C) enabled rapid in-situ thermal drying of the ethanol solvent, eliminating the need for forced convection (e.g., an air knife). Subsequently, the coated HTL was thermally annealed at 100 °C for 5 min. Following the HTL deposition, the perovskite precursor solution was deposited using the slot-die coating with the substrate temperature maintained at 40 °C. Immediately after coating, the wet perovskite films were quickly transferred into a vacuum chamber for a vacuum flash-assisted drying process. The chamber pressure was rapidly evacuated to approximately 10 Pa within 20 s. This vacuum extraction accelerates solvent removal and induces a rapid supersaturation, leading to uniform intermediate phase formation. Subsequently, the films were thermally annealed on a hot plate at 150 °C for 10 min. Finally, the TEACl passivation layer and the $PC_{61}BM$ ETL were sequentially deposited via slot-die coating under optimized conditions to complete the large-area functional layers. For perovskite solar module (PSM) fabrication, the FTO substrates were first divided into individual sub-cells by P1 laser patterning using a 1064 nm laser, with a scribing pitch of 0.5 cm. After sequential deposition of all functional layers excluding the top metal contact, P2 laser scribing was carried out with a 532 nm wavelength to define the interconnection region. Subsequently, a silver electrode with a thickness of 120 nm was deposited via thermal evaporation. The series-connected module architecture was finalized by forming the P3 scribe using a 532 nm laser.

2.3. Characterization methods

To evaluate the surface electronic properties of the modified coatings, the work function was characterized using Kelvin probe force microscopy (KPFM, SKP5050, KP Technology Ltd.). Surface wettability and coating homogeneity were assessed by measuring the water contact angle using an automatic goniometer (DMo-602, Kyowa). To account for data variability, measurements were performed at five independent locations on each sample surface (n = 5). All results are presented as the mean ± standard deviation (SD). To investigate the film quality and defect passivation effects, steady-state photoluminescence (PL) and time-resolved photoluminescence (TRPL) spectra were measured using a fluorescence spectrophotometer (FLS1000, Edinburgh Instrument). Chemical bonding and functional group variations at the SAMs interface were analyzed using a Fourier-transform infrared spectrometer (FTIR; FT/lR-6X, Jasco). Surface morphology of the samples was characterized by Atomic Force Microscopy (AFM; XE70, Park) to evaluate film surface characteristics. To ensure consistency, both interfacial charge transport behavior and device performance were investigated using the complete device architecture, which was configured as follows: FTO glass/ HTL/ Perovskite/ TEACl/ PCBM/ BCP/ Ag. Interfacial charge transport behavior was investigated through transient photovoltage (TPV) and transient photocurrent (TPC) analyses performed on a PAIOS measurement platform (Fluxim). For TPV, the devices were maintained under open-circuit conditions and subjected to a short optical pulse to monitor the transient voltage response. In contrast, TPC measurements were recorded under short-circuit conditions to observe the photocurrent decay over time. Finally, the functional performance of the coatings within the device architecture was validated by measuring the current density-voltage (J–V) characteristics using a source meter (Keithley 2410) under simulated AM 1.5 G illumination supplied by a calibrated solar simulator (SS-X100R AAA, Enlitech).

3. Results and discussion

A systematic investigation was conducted to elucidate the influence of carboxylic acid additives on the coating formation and electronic properties of SAMs. Given that dipole orientation and molecule–substrate interactions critically define the energetic landscape of HTL surfaces, this study focuses on understanding how carboxylic acid additives affect both the intrinsic dipole of SAM molecules and the interfacial dipole generated upon binding to the substrate. Specifically, we aim to clarify how these additives regulate SAM packing, anchoring configurations, and the resulting shifts in the HTL vacuum level. Therefore, we selected two simple carboxylic acid derivatives, acetic acid (AcOH) and trifluoroacetic acid (TFA). Owing to their distinct electron-withdrawing strengths and molecular dipoles, these additives provide an effective model system for assessing how subtle chemical variations translate into differences in interfacial energetics and film quality. As shown in Fig. 1**(a)**, the two molecules exhibit markedly different polarities, which are expected to alter the total interfacial dipole when incorporated into the MeO-2PACz layer. Through comparative analysis, we disentangle how acidity and dipole orientation govern SAM self-assembly behavior and, ultimately, the work function of the HTL surface. To evaluate the impact of dipole modulation, we examined the work function evolution of MeO-2PACz layers using KPFM. Measurements were performed on SAM-modified FTO substrates prepared with varying additive concentrations, as shown in Fig. 1**(b)**. Because AcOH and TFA possess dipole moments oriented in opposite directions, SAMs prepared with AcOH exhibit a reduced work function, whereas those prepared with TFA show an increased work function. This tunable behavior demonstrates that dipole-engineered small-molecule additives provide an efficient means to modulate the surface potential of SAM-coated FTO substrates. Specifically, a positive dipole shifts the vacuum level upward, leading to a higher MeO-2PACz work function and improved energy-level alignment with the perovskite HOMO [26]. To assess the scalability of the TFA modification, we evaluated the work-function (WF) uniformity across a 4 × 4 cm^2 substrate, divided into four quadrants **(Figure S1(a))**. As shown in **Figure S1(b)**, while large-area coating kinetics induce slight variations in the absolute WF values compared to small-area samples, incorporating 2 mM TFA into the MeO-2PACz solution reliably produces a uniform ΔWF shift across the entire surface. This consistent macroscopic dipole modulation confirms the robustness of the additive-engineered interface and its compatibility with scalable perovskite photovoltaic fabrication. The corresponding energy-level diagram is shown in Fig. 1**(c)**. In addition, we evaluated the coating uniformity of MeO-2PACz by measuring the water contact angle of the modified films (Fig. 1**(d)**). While TFA effectively tunes the work function through its dipole orientation, its incorporation also enhances the macroscopic uniformity of the MeO-2PACz layer. The water contact angle increased from 55.7 ± 1.1° to 67.4 ± 1.2°, indicating improved surface hydrophobicity and more complete molecular coverage. These results suggest that TFA-assisted molecular assembly promotes a denser and more uniform MeO-2PACz film, eliminating surface pinholes which is crucial for high-yield coating processes [27]. Furthermore, this improvement implies that the introduction of small carboxylic acid molecules can regulate the molecular aggregation of the MeO-2PACz SAM, leading to a more ordered packing configuration and reduced local disorder within the monolayer. To confirm the presence of TFA within the film after processing, FTIR spectroscopy was conducted on the annealed samples. As shown in **Figure S2,** the TFA-treated film exhibits a distinct C=O stretching vibration peak at ~1710 cm^{-1}, alongside intense C–F stretching bands (1150–1200 cm^{-1}) and a massive hydrogen-bonded O-H bending valley (~900 cm^{-1}) [28, 29]. The simultaneous persistence of these characteristic signals confirms that intact TFA molecules are strongly coordinated at the interface, rather than being completely removed through volatilization or thermal decomposition. Such robust adsorption indicates that TFA does not merely act as a transient processing additive but remains functionally active at the interface, facilitating defect passivation and enhancing interfacial contact. By leveraging such carboxylic acid additives, we can finely adjust the SAM-induced work function within a practical range without redesigning the SAM molecules themselves. This strategy significantly lowers research and material development costs while offering excellent process compatibility and scalability.

To validate the functional integrity and electronic quality of the

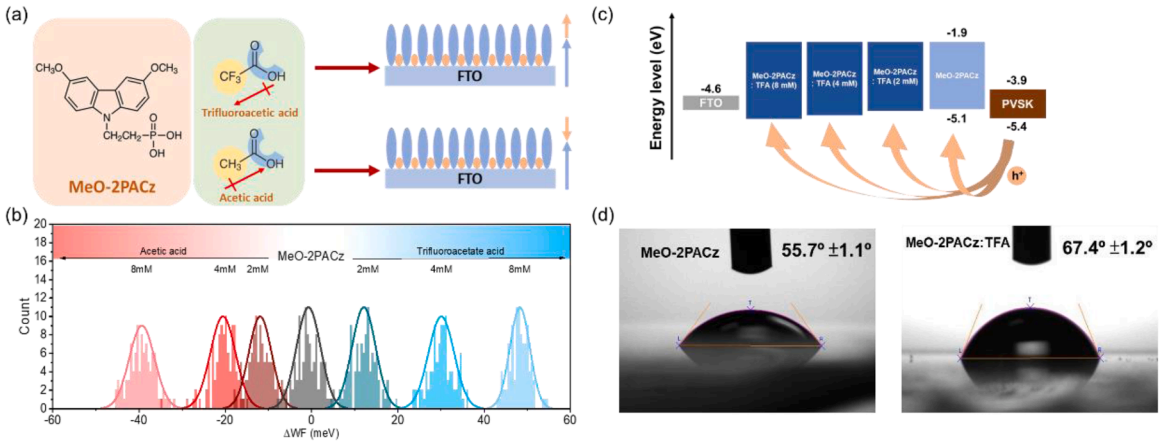

Fig. 1. (a) Schematic illustration of MeO-2PACz modified with carboxylic acid additives. (b) Distributions of work function shifts (ΔWF) for MeO-2PACz films treated with acetic acid (AcOH; 2, 4, and 8 mM) and trifluoroacetic acid (TFA; 2, 4, and 8 mM). (c) Energy-level alignment diagram of pristine FTO and HTL-modified FTO relative to the PVSK layer. (d) Water contact angle of MeO-2PACz and MeO-2PACz:TFA films; data are presented as the mean ± SD calculated from 5 independent measurements at distinct locations.

deposited coatings, we fabricated inverted PSC devices with the structure FTO/SAMs/perovskite/PCBM/BCP/Ag, using the modified SAMs as the hole-transporting interface. The photovoltaic parameters, which serve as a direct indicator of the coating's uniformity and defect density, are summarized in Table 1, with statistical distributions presented in Fig. 2. The control device (without TFA) achieves a PCE of 19.97%, with a V_{OC} of 1.17 V, a J_{SC} of 21.53 mA/cm^2, and an FF of 79.21%. Upon introducing TFA at different concentrations, a pronounced enhancement in device performance is observed. Notably, the device incorporating 2 mM TFA exhibits a champion PCE of 22.18%, accompanied by a V_{OC} of 1.17 V, a J_{SC} of 23.84 mA/cm^2, an FF of 79.47%. As shown in Fig. 2, while the V_{OC} and FF remained relatively stable, the J_{SC} showed a substantial increase from 21.53 to 23.84 mA/cm^2 upon optimal TFA addition. This improvement provides strong evidence that TFA effectively improves the surface coverage and uniformity of the MeO-2PACz HTL, aligning well with the contact angle results. This enhanced coverage minimizes interfacial shunts and facilitates more efficient hole extraction, confirming that the optimized coating morphology translates directly into superior electronic performance. Furthermore, compared to the sequential deposition method (**Figure S3**), the mixed solution strategy enables simultaneous molecular anchoring, which prevents potential damage to the pre-assembled SAM layer by the second solvent and yields a more robust additive-engineered interface. In addition, we investigated the morphological evolution of films via AFM. As shown in **Figure S4(a)**, the surface roughness of the pristine MeO-2PACz layer increases slightly with TFA concentration, with the root-mean-square (RMS) roughness rising from 25.83 to 26.79 nm. This is likely due to perturbed molecular self-assembly induced by excessive additives. Conversely, the subsequent perovskite layer exhibits a smoother morphology upon optimal TFA incorporation, with the RMS roughness decreasing from 16.34 to 15.08 nm (**Figure S4(b)**). This improved surface uniformity not only ensures intimate interfacial contact for subsequent upper layer deposition but also suppresses localized charge accumulation, thereby facilitating efficient charge extraction and enhancing overall device performance.

Table 1
Photovoltaic parameters of devices fabricated with different TFA concentrations. Average values are obtained from 20 devices, with highest data provided in parentheses.

Concentration of TFA (mM)	V_{OC} (V)	J_{SC} (mA/cm^2)	FF (%)	PCE (%)
0	1.16±0.01 (1.17)	21.42±0.33 (21.53)	75.73±2.77 (79.21)	18.84±0.83 (19.97)
1	1.16±0.00 (1.17)	22.05±0.27 (22.38)	79.99±0.64 (80.77)	20.47±0.32 (21.07)
2	1.16±0.01 (1.17)	23.15±0.39 (23.84)	78.29±1.13 (79.47)	21.05±0.68 (22.18)
4	1.16±0.01 (1.15)	22.11±0.24 (22.50)	79.03±0.86 (80.24)	20.27±0.42 (20.84)

Beyond the statistical distributions, the current density-voltage (J–V) curves for the champion devices, presented in Fig. 3**(a)**, provide direct confirmation of the functional enhancement induced by TFA-modified coating. To investigate the mechanism behind this improvement, steady-state PL measurements were performed to probe the interfacial coating quality. As shown in Fig. 3**(b)**, the perovskite film deposited on the TFA-modified HTL exhibits a significantly higher PL intensity compared to the control. This enhancement indicates that the denser and more uniform TFA-modified SAM coating effectively passivates interfacial defects. Consistent with established comprehensive photophysical models, such effective passivation significantly mitigates trap-assisted non-radiative recombination pathways at the buried interface, thereby enhancing the overall radiative recombination efficiency [30–32]. To systematically elucidate the charge carrier dynamics, reflecting the physical quality of the interface, TPC and TPV measurements were employed. The corresponding carrier recombination and extraction lifetimes are summarized in Table 2. The TPV and TPC results, as shown in Fig. 3**(c)**, indicate that the incorporation of TFA significantly prolongs the carrier recombination lifetime from 3.31 ms to 6.29 ms. Concurrently, TPC measurements (Fig. 3**(c)**) show a reduction in charge extraction time from 0.84 μs to 0.71 μs. These results suggest a dual benefit of the optimized coating: it minimizes non-radiative recombination sites while facilitating faster hole collection through a defect-free contact [33,34]. Furthermore, light-intensity-dependent V_{OC} and J_{SC} measurements were conducted to analyze the recombination kinetics (Fig. 3**(d)**), and the relationship between V_{OC} and light intensity follows the established literature model [35]. As detailed in Table 2, the device utilizing the TFA-modified coating shows a decrease in the ideality factor (n) from 1.49 to 1.13. This reduction strongly indicates that trap-assisted recombination is effectively suppressed, directly attributable to the improved surface coverage and reduced defect density of the SAM layer. These results confirm that TFA-assisted assembly creates an energetically favorable and physically robust interface, which directly accounts for the superior electronic performance.

Building on the mechanistic understanding of how TFA enhances the quality of MeO-2PACz films, we validated the process transferability from lab-scale spin-coating to industrial slot-die coating, a critical step for advancing coating technologies toward commercialization. To this end, we compare functional quality of SAM coating deposited by the two

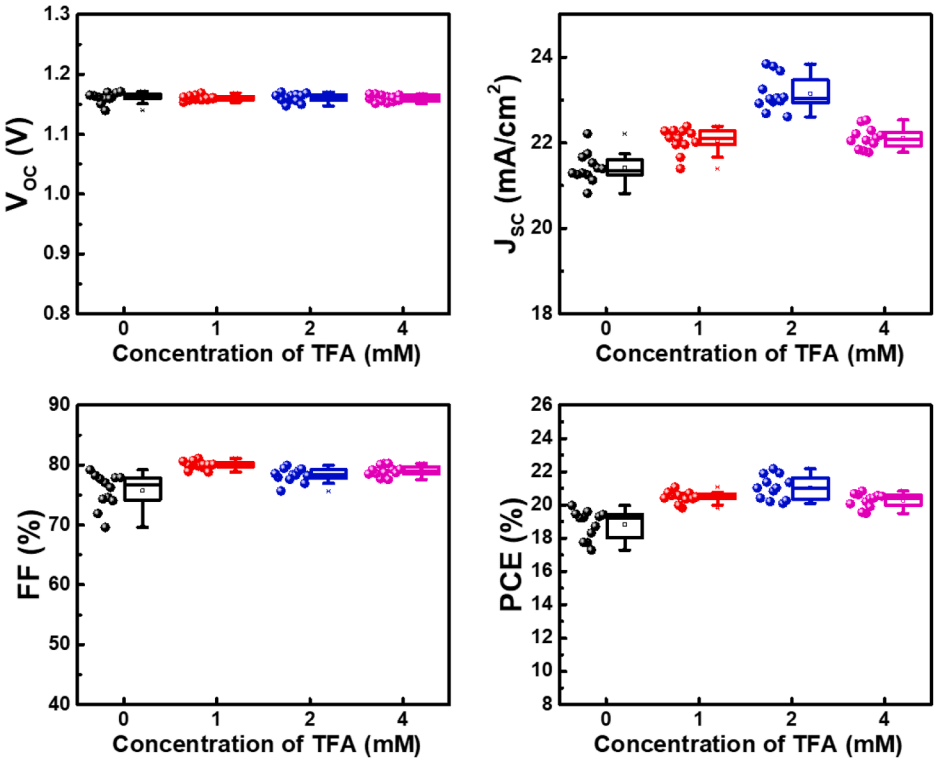

Fig. 2. Statistical distributions of photovoltaic parameters (V_{OC}, J_{SC}, FF, and PCE) for PSCs fabricated with different TFA concentrations (0, 1, 2, and 4 mM). The box plots represent data collected from 20 independent devices.

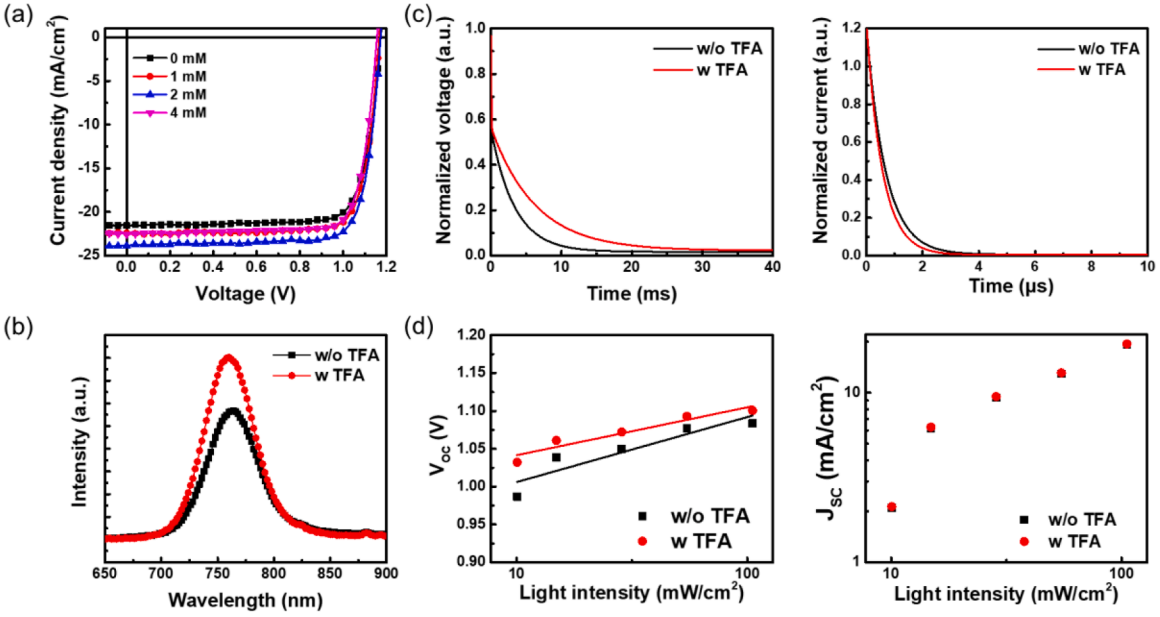

Fig. 3. (a) J-V characteristics of PSCs fabricated with different TFA concentrations (0, 1, 2, and 4 mM). (b) Steady-state PL spectra of perovskite films without and with TFA (2 mM). (c) Transient photovoltage (TPV) and transient photocurrent (TPC) responses of PSCs without and with TFA. (d) Light-intensity–dependent V_{OC} and J_{SC} curves used to extract the ideality factor (n) and the α value, respectively.

distinct methods. The statistical photovoltaic distributions of PSCs are presented in Fig. 4**(a)**, with details summarized in Table 3. While slot-die coated devices typically exhibit slightly lower efficiencies than their spin-coated devices due to differences in drying kinetics, the incorporation of TFA significantly narrows this performance gap. Notably, the enhancement in J_{SC} observed in spin-coated devices does not fully translate to the slot-die process. We attribute this to the rapid in-situ thermal drying on the heated substrate, which kinetically traps the molecules to ensure macroscopic film uniformity but restricts the time window for optimal micro-scale molecular self-assembly. Consequently, in the scalable slot-die process, the primary contribution of TFA shifts toward interfacial defect passivation rather than further boosting charge extraction, which accounts for the preserved enhancements in V_{OC} and FF. The TFA-modified slot-die PSCs achieved a champion PCE of

Table 2
Charge-carrier dynamics and electrical characteristics of PSCs fabricated without and with TFA.

TFA	Carrier recombination time (ms)	Carrier extraction time (μs)	n	α
w/o	3.31	0.84	1.49	0.91
w	6.29	0.71	1.13	0.91

17.60%, showing a marked improvement over the control PSCs (16.93%). More importantly, the standard deviation of the PCE decreased from 1.06 to 0.68. This reduction serves as a key indicator that TFA improves the coating uniformity and process reproducibility over large areas, effectively mitigating drying-induced defects. To comprehensively evaluate device durability, we monitored the long-term stability of unencapsulated cells under ambient conditions (55% RH, 25 °C). As presented in **Figure S5(a)**, the TFA-modified devices exhibited superior environmental resilience, retaining 91% of their initial PCE after 200 h of exposure. Furthermore, long-term operational stability was assessed through continuous maximum power point (MPP) tracking under constant illumination provided by an LED solar simulator (LSH-7320) in ambient air (**Figure S5(b)**). The TFA-treated devices maintained a significantly more stable power output compared to the control. To further assess the environmental robustness of the TFA-engineered SAM, we conducted accelerated aging tests on unencapsulated PSCs under ISOS-D-2 conditions (65 °C, 40% RH). As shown in Fig. 4**(b)**, the devices incorporating TFA retained 65% of their initial PCE after 120 h of thermal and humidity stress, exhibiting superior stability compared to the control PSCs. This enhanced durability is attributed to the denser molecular packing of the coating, which effectively prevents moisture ingress and suppresses interfacial degradation. Finally, to demonstrate the feasibility of this strategy for industrial applications, we fabricated 5 × 5 cm^2 perovskite solar modules (PSMs) using the TFA-assisted slot-die coating process. The modules were patterned with a P1-P2-P3 laser scribing process (active area: 7.0 cm^2). Fig. 4**(c)** presents the J–V characteristics, and the parameters are summarized in Table 4. The control PSM exhibits a PCE of 12.63%, with a V_{OC} of 5.10 V, a J_{SC} of 3.42 mA/cm^2, and a FF of 72.47%. In contrast, the TFA-modified PSM delivered a significantly improved PCE of 14.72%, with a V_{OC} of 5.44 V, a J_{SC} of 3.53 mA/cm^2, and an FF of 76.63%. These results confirm that TFA-assisted SAM engineering is fully compatible with scalable fabrication processes, verifying that the molecular-level benefits are effectively translated into high-quality and large-area functional coatings. **Table S1** compares the performance of our work with current state-of-the-art PSCMs, indicating its competitive performance.

4. Conclusions

In this work, we systematically demonstrated a dipole engineering strategy to enhance both the electronic properties and coating uniformity of ultrathin SAM films. We show that the dipole orientation and electron-withdrawing strength of carboxylic acid additives, specifically TFA, play a decisive role in determining the molecular packing of MeO-2PACz SAMs and the resulting interfacial dipole. Functionally, TFA induces a downward shift of the SAM-induced HOMO level, optimizing the energy-level alignment between the HTL and perovskite absorber.

Table 3
Photovoltaic characteristics of PSCs employing HTL fabricated using different deposition processes.

Process	TFA	V_{OC} (V)	J_{SC} (mA/cm^2)	FF (%)	PCE (%)
Spin (SP)	w/o	1.13±0.03 (1.18)	19.83±0.22 (20.85)	75.7 ± 2.72 (76.49)	16.91±0.57 (18.89)
	w	1.18±0.01 (1.18)	23.47±0.43 (23.82)	76.9 ± 1.36 (79.18)	21.32±0.59 (22.35)
Slot-die (SD)	w/o	1.04±0.07 (1.08)	18.82±0.69 (18.83)	79.93±2.80 (83.07)	15.63±1.06 (16.93)
	w	1.10±0.02 (1.12)	18.76±0.61 (18.88)	81.62±1.76 (82.95)	16.91±0.68 (17.60)

Table 4
Photovoltaic parameters of slot-die based PSMs fabricated without and with TFA.

TFA	V_{OC} (V)	J_{SC} (mA/cm^2)	FF (%)	PCE (%)
w/o	5.10	3.42	72.47	12.63
w	5.44	3.53	76.63	14.72

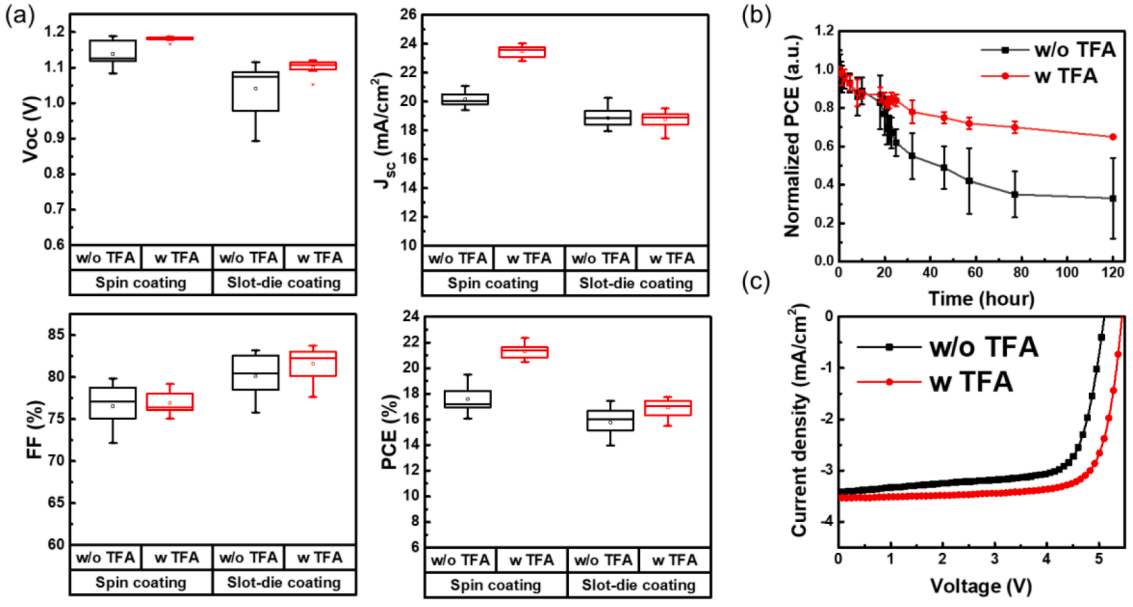

Fig. 4. (a) Statistical distributions of device performance for HTLs deposited by spin-coating and slot-die coating. The box plots represent data collected from 18 independent devices. (b) Storage stability of unencapsulated PSCs measured for 25 h under ISOS-D-2 condition. (c) J-V characteristics of the champion PSMs fabricated without and with TFA.

Structurally, the increased water contact angle and improved film morphology indicate that TFA promotes denser and more uniform molecular coverage, which effectively suppresses trap formation and facilitates efficient hole extraction. Crucially, we successfully translated these benefits from lab-scale spin-coating to scalable slot-die coating processes. The TFA-modified slot-die coatings exhibited significantly improved reproducibility, narrowing the efficiency gap with spin-coated devices. Furthermore, the robustness of this strategy was validated in large-area 5 × 5 cm^2 perovskite solar modules, achieving a PCE of 14.72% and enhanced operational stability under thermal and humidity stress. Overall, our findings establish TFA-assisted SAM engineering as a process-compatible, cost-effective, and scalable approach. By enabling precise control over interfacial energetics while simultaneously improving coating quality, this strategy effectively addresses key bottlenecks in large-area manufacturing, paving the way for the commercialization of stable and efficient perovskite solar technologies.

CRediT authorship contribution statement

Chia-Feng Li: Writing – original draft, Validation, Methodology, Investigation, Formal analysis, Data curation. **Shih-Han Huang:** Writing – review & editing, Formal analysis. **Sheng-Wen Huang:** Investigation, Formal analysis, Data curation. **You-Ren Chen:** Investigation, Data curation. **Hou-Chin Cha:** Investigation, Funding acquisition, Formal analysis. **Pin-Hao Chao:** Validation, Investigation, Data curation. **Feng-Yu Tsai:** Supervision, Resources. **Yu-Ching Huang:** Writing – review & editing, Supervision, Resources, Project administration, Funding acquisition, Conceptualization.

Declaration of competing interest

The authors declare the following financial interests/personal relationships which may be considered as potential competing interests: Yu-Ching Huang reports financial support was provided by National Science and Technology Council of Taiwan. If there are other authors, they declare that they have no known competing financial interests or personal relationships that could have appeared to influence the work reported in this paper.

Acknowledgment

Financial supports provided by the National Science and Technology Council of Taiwan (Grant Nos. NSTC 111-2923-E-002-012-MY3; NSTC 111-2221-E-002-026-MY3, NSTC 112-2628-E–131-001-MY4, NSCT 113-2218-E-002-026-, NSTC 114-2218-E-002-016-, NSTC 114-2221-E-002-045-, NSTC 114-2222-E–131-002-, NSTC 114-2622-E–131-007-, NSTC 114-2622-E–131-015-, and NSTC 114-2221-E–131-012-MY3) are highly appreciated. This work was partially supported by “Advanced Research Center for Green Materials Science and Technology” from The Featured Area Research Center Program within the framework of the Higher Education Sprout Project by the Ministry of Education (Grant No 114L9006).

Supplementary materials

Supplementary material associated with this article can be found, in the online version, at doi:10.1016/j.surfin.2026.109929.

Data availability

Data will be made available on request.

References

[1] Z. Li, T.R. Klein, D.H. Kim, M. Yang, J.J. Berry, M.F. Van Hest, K. Zhu, Scalable fabrication of perovskite solar cells, Nat. Rev. Mater. 3 (4) (2018) 1–20, https://doi.org/10.1038/natrevmats.2018.17.
[2] S.H. Huang, C.K. Guan, P.H. Lee, H.C. Huang, C.F. Li, Y.C. Huang, W.F. Su, Toward all slot-die fabricated high efficiency large area perovskite solar cell using rapid near infrared heating in ambient air, Adv. Energy Mater. 10 (37) (2020) 2001567, https://doi.org/10.1002/aenm.202001567.
[3] NREL. https://www.nrel.gov/pv/cell-efficiency.html, 2026.
[4] K. Almasabi, X. Zheng, B. Turedi, A.Y. Alsalloum, M.N. Lintangpradipto, J. Yin, L. Gutierrez-Arzaluz, K. Kotsovos, A. Jamal, I. Gereige, Hole-transporting self-assembled monolayer enables efficient single-crystal perovskite solar cells with enhanced stability, ACS Energy Lett. 8 (2) (2023) 950–956, https://doi.org/10.1021/acsenergylett.2c02333.
[5] A. Farag, T. Feeney, I.M. Hossain, F. Schackmar, P. Fassl, K. Küster, R. Bäuerle, M. A. Ruiz-Preciado, M. Hentschel, D.B. Ritzer, Evaporated self-assembled monolayer hole transport layers: lossless interfaces in p-i-n perovskite solar cells, Adv. Energy Mater. 13 (8) (2023) 2203982, https://doi.org/10.1002/aenm.202203982.
[6] D. Yeo, J. Shin, D. Kim, J.Y. Jaung, I.H. Jung, Self-assembled monolayer-based hole-transporting materials for perovskite solar cells, Nanomaterials 14 (2) (2024) 175, https://doi.org/10.3390/nano14020175.
[7] S. Wang, D. Khan, W. Zhou, Y. Sui, T. Zhang, G. Yu, Y. Huang, X. Yang, X. Chen, H. Yan, J. Tang, F. Yang, P. Han, Z. Zheng, Y. Zhang, Z. Tang, Ion-dipole interaction for self-assembled monolayers: a new strategy for buried interface in inverted perovskite solar cells, Adv. Funct. Mater. 34 (27) (2024) 2316202, https://doi.org/10.1002/adfm.202316202.
[8] L. Cao, Y. Tong, Y. Ke, W. Zhang, T. Li, Z. Kang, H. Wang, K. Wang, Modification of nickel oxide via self-assembled monolayer for enhanced performance of air-processed FAPbI3 perovskite solar cells, ACS Appl. Energy Mater. 7 (4) (2024) 1508–1516, https://doi.org/10.1021/acsaem.3c02777.
[9] Y. Yang, X. Shi, A.N. Stein, M.R. Lockett, J. Huang, Understanding phosphonic-acid molecules based hole transport layers in perovskite solar cells, Adv. Energy Mater. 16 (7) (2026) e05937, https://doi.org/10.1002/aenm.202505937.
[10] W. Liu, R. Chen, Z. Tan, J. Wang, S. Liu, C. Shi, X. Liu, Y. Cai, F. Ren, Z. Zhou, Q. Zhou, W. Li, T. Miao, H. Zhu, T. Imran, Z. Liu, W. Chen, Buried interface engineering for scalable processing of high-performance inverted perovskite solar modules, Adv. Energy Mater. 15 (13) (2025) 2404374, https://doi.org/10.1002/aenm.202404374.
[11] S. Fu, N. Sun, H. Chen, Y. Li, Y. Li, X. Zhu, B. Feng, X. Guo, C. Yao, W. Zhang, Homogenizing SAM deposition via seeding–OH groups for scalable fabrication of perovskite solar cells, Energy Environ. Sci. 18 (7) (2025) 3305–3312, https://doi.org/10.1039/D5EE00350D.
[12] J. Wang, B. Jiao, R. Tian, K. Sun, Y. Meng, Y. Bai, X. Lu, B. Han, M. Yang, Y. Wang, Less-acidic boric acid-functionalized self-assembled monolayer for mitigating NiOx corrosion for efficient all-perovskite tandem solar cells, Nat. Commun. 16 (1) (2025) 4148, https://doi.org/10.1038/s41467-025-59515-6.
[13] X. Wang, J. Li, R. Guo, X. Yin, R. Luo, D. Guo, K. Ji, L. Dai, H. Liang, X. Jia, Regulating phase homogeneity by self-assembled molecules for enhanced efficiency and stability of inverted perovskite solar cells, Nat. Photonics 18 (12) (2024) 1269–1275, https://doi.org/10.1038/s41566-024-01531-x.
[14] R. Guo, X. Zhang, X. Zheng, L. Li, M. Li, Y. Zhao, S. Zhang, L. Luo, S. You, W. Li, Z. Gong, R. Huang, Y. Cui, Y. Rong, H. Zeng, X. Li, Tailoring multifunctional self-assembled hole transporting molecules for highly efficient and stable inverted perovskite solar cells, Adv. Funct. Mater. 33 (10) (2023) 2211955, https://doi.org/10.1002/adfm.202211955.
[15] Y. Zhang, Y. Tang, Z. Zhang, J. Zhao, H. Wu, Z. Li, J. Yang, Y. Zhou, Z. Su, H. Liu, M. Li, A π-conjugated molecular bridge strategy for constructing efficient hole transport pathways in inverted perovskite solar cells, Angew. Chem. Int. Ed. 64 (44) (2025) e202514640, https://doi.org/10.1002/anie.202514640.
[16] C. Luo, Q. Zhou, K. Wang, X. Wang, J. He, P. Gao, C. Zhan, Z. Bi, W. Li, Y. Ma, W. Chen, Y. Hou, Z. Liu, Q. Zhao, Engineering bonding sites enables uniform and robust self-assembled monolayer for stable perovskite solar cells, Nat. Mater. 24 (8) (2025) 1265–1272, https://doi.org/10.1038/s41563-025-02275-x.
[17] T. Liu, C. Luo, R. He, Z. Zhang, X. Lin, Y. Chen, T. Wu, Advancing self-assembled molecules toward interface-optimized perovskite solar cells: from one to two, Adv. Mater. 37 (48) (2025) 2502032, https://doi.org/10.1002/adma.202502032.
[18] J. Ding, G. Li, Q. Tang, H. Liu, Z. Wang, I. Santoso, T. Chen, C. Chen, Molecular doping of self-assembled monolayers for interface engineering in inverted perovskite solar cells and large-area bifacial modules: enhancing uniformity, crystallization, and stability, Adv. Energy Mater. 15 (43) (2025) e03252, https://doi.org/10.1002/aenm.202503252.
[19] R. He, X. Liu, T. Liu, T. Zhao, Y. Chen, Q. Song, Precisely-controlled Co-self-assembled monolayer for improved performance of blade-coated perovskite solar cells, Adv. Funct. Mater. 35 (39) (2025) 2506386, https://doi.org/10.1002/adfm.202506386.
[20] L. Zhang, M. Fu, X. Jiang, Z. Zhang, C. Wang, Z. Su, B. He, L. Tang, G. Zheng, X. Gao, J. He, Benzylphosphonic acid-engineered compact self-assembled monolayers for bifacial buried interface passivation in high-performance inverted perovskite solar cells, Adv. Sci. 12 (45) (2025) e12117, https://doi.org/10.1002/advs.202512117.
[21] D. Li, Q. Lian, T. Du, R. Ma, H. Liu, Q. Liang, Y. Han, G. Mi, O. Peng, G. Zhang, W. Peng, B. Xu, X. Lu, K. Liu, J. Yin, Z. Ren, G. Li, C. Cheng, Co-adsorbed self-assembled monolayer enables high-performance perovskite and organic solar cells, Nat. Commun. 15 (1) (2024) 7605, https://doi.org/10.1038/s41467-024-51760-5.

[22] Q. Cao, T. Wang, X. Pu, X. He, M. Xiao, H. Chen, L. Zhuang, Q. Wei, H.L. Loi, P. Guo, Co-self-assembled monolayers modified NiOx for stable inverted perovskite solar cells, Adv. Mater. 36 (16) (2024) 2311970, https://doi.org/10.1002/adma.202311970.

[23] E.J. Cassella, E.L.K. Spooner, T. Thornber, M.E. O'Kane, T.E. Catley, J.E. Bishop, J. A. Smith, O.S. Game, D.G. Lidzey, Gas-assisted spray coating of Perovskite solar cells incorporating sprayed self-assembled monolayers, Adv. Sci. 9 (14) (2022) 2104848, https://doi.org/10.1002/advs.202104848.

[24] E. Parvazian, R. Garcia-Rodriguez, D. Beynon, M. Davies, T. Watson, Slot-die coating of self-assembled monolayers: a scalable approach for perovskite solar cells, Mater. Today Energy 52 (2025) 101955, https://doi.org/10.1016/j.mtener.2025.101955.

[25] Y.-C. Huang, S.-W. Huang, C.-F. Li, S.-H. Huang, F.-Y. Tsai, W.-F. Su, A comprehensive optimization of highly efficient MA-free wide-bandgap perovskites for 4-T Perovskite/Silicon tandem solar cells, Chem. Eng. J. 503 (2025) 158272, https://doi.org/10.1016/j.cej.2024.158272.

[26] L. Canil, T. Cramer, B. Fraboni, D. Ricciarelli, D. Meggiolaro, A. Singh, M. Liu, M. Rusu, C.M. Wolff, N. Phung, Q. Wang, D. Neher, T. Unold, P. Vivo, A. Gagliardi, F. De Angelis, A. Abate, Tuning halide perovskite energy levels, Energy Environ. Sci. 14 (3) (2021) 1429–1438, https://doi.org/10.1039/D0EE02216K.

[27] C. Bi, Q. Wang, Y. Shao, Y. Yuan, Z. Xiao, J. Huang, Non-wetting surface-driven high-aspect-ratio crystalline grain growth for efficient hybrid perovskite solar cells, Nat. Commun. 6 (1) (2015) 7747, https://doi.org/10.1038/ncomms8747.

[28] G. Turrin, J. Crugeiras, C. Bisquoli, D. Barboni, M. Catani, B. Rodríguez-Meana, R. Boaretto, M. Albicini, S. Caramori, C. Trapella, T. Stieglitz, Y. Baslan, H. Karlsson-Fernberg, F.L. Narvaez-Chicaiza, E. Marchini, A. Cavazzini, R. López-Vales, M. Asplund, X. Navarro, S. Carli, Covalent binding of dexamethasone to polyimide improves biocompatibility of neural implantable devices, Adv. Heal Mater. 14 (21) (2025) 2405004, https://doi.org/10.1002/adhm.202405004.

[29] L. Ren, P. Huang, W. Chen, Y. Chen, Z. Gao, W. Lv, Y. Li, Reversible thermally driven phenyl torsion in self-assembled monolayers releases strain for heat-resilient inverted perovskite solar cells, Angew. Chem. 138 (2) (2026) e21774, https://doi.org/10.1002/ange.202521774.

[30] I. Levine, A. Al-Ashouri, A. Musiienko, H. Hempel, A. Magomedov, A. Drevilkauskaite, V. Getautis, D. Menzel, K. Hinrichs, T. Unold, S. Albrecht, T. Dittrich, Charge transfer rates and electron trapping at buried interfaces of perovskite solar cells, Joule 5 (11) (2021) 2915–2933, https://doi.org/10.1016/j.joule.2021.07.016.

[31] G. Qu, S. Cai, Y. Qiao, D. Wang, S. Gong, D. Khan, Y. Wang, K. Jiang, Q. Chen, L. Zhang, Y.-G. Wang, X. Chen, A.K.Y. Jen, Z.-X. Xu, Conjugated linker-boosted self-assembled monolayer molecule for inverted perovskite solar cells, Joule 8 (7) (2024) 2123–2134, https://doi.org/10.1016/j.joule.2024.05.005.

[32] R. Yin, W. Miao, K. Wang, W. Liu, W. Sun, J. Lv, Z. Dong, T. You, W. Hao, P. Yin, Coassembled self-assembled monolayers enable efficient and stable inverted perovskite solar cells, ACS Nano 19 (47) (2025) 40345–40353, https://doi.org/10.1021/acsnano.5c07208.

[33] J. Shi, Y. Li, Y. Li, D. Li, Y. Luo, H. Wu, Q. Meng, From ultrafast to ultraslow: charge-carrier dynamics of perovskite solar cells, Joule 2 (5) (2018) 879–901, https://doi.org/10.1016/j.joule.2018.04.010.

[34] Z. Xu, X. Sun, W. Hui, Q. Wang, P. Xu, W. Tang, H. Hu, L. Song, X. Xu, Y. Wu, Q. Peng, Optimizing molecular packing and interfacial contact via halogenated N-glycidyl carbazole small molecules for low energy loss and highly efficient inverted perovskite solar cells, Angew. Chem. Int. Ed. 64 (26) (2025) e202503008, https://doi.org/10.1002/anie.202503008.

[35] D. Liu, C. Chen, X. Wang, X. Sun, B. Zhang, Q. Zhao, Z. Li, Z. Shao, X. Wang, G. Cui, S. Pang, Enhanced quasi-fermi level splitting of perovskite solar cells by universal dual-functional polymer, Adv. Mater. 36 (13) (2024) 2310962, https://doi.org/10.1002/adma.202310962.